Planetary and Space Science 220 (2022) 105533

Contents lists available at ScienceDirect

Planetary and Space Science

journal homepage: www.elsevier.com/locate/pss

Asteroid regolith strength: Role of grain size and surface properties

Julie Brisset [a,*], Paul Sánchez [b], Christopher Cox [a], Dennis Corraliza [a], John Hatchitt [a], Alexander Madison [a], Thomas Miletich [a]

[a] Florida Space Institute, University of Central Florida, 12354 Research Parkway, Orlando, FL, 32826, USA
[b] Colorado Center for Astrodynamics Research, The University of Colorado Boulder, 3775 Discovery Drive, Boulder, CO, 80303, USA

A B S T R A C T

Most of the small asteroids with sizes below a few km are believed to be rubble piles. In order to study the strength of such bodies, we have performed bulk measurements on simulant granular material, varying the grain size and surface properties in ambient conditions. The samples were prepared from a high-fidelity asteroid soil simulant and subjected to compression and shear stresses. We measured the material angle of repose, Young Modulus, its angle of internal friction, bulk cohesion, and tensile strength. Grain sizes were varied from 0.1 to 10 mm. Grain surface properties (friction and cohesive forces) were modified by adding a surface frost layer. We find that, in shear, larger grains increase the strength in confined samples, representative of regolith subsurface layers on asteroids, while they decrease strength in unconfined samples, representative of surface regolith. In compression, confined samples become weaker with increasing grain size, while unconfined samples are barely sensitive to it. We also find that increasing surface friction and intergrain cohesion increases the strength in all the samples. We measure bulk cohesion values between ~400 and 600 Pa, internal friction between 25 and 45°, and tensile strengths between 600 and 900 Pa. The measured angles of repose varied between ~25 and 45° in an opposite trend to the internal friction. We compare these values to spacecraft data and numerical simulations and discuss implications of our findings for rubble-pile composition and disintegration behavior. We find that grain size sorting with depth, depletion of fines at the surface, or presence of water ice in the core can provide a mechanism for regular surface shedding event on small asteroids.

1. Introduction

The study of small bodies of the Solar System is key to understanding the formation and evolution of our planetary system. The smaller, undifferentiated members of the various small body populations (Near Earth Objects, Main Belt Asteroids, Jupiter Family Comets, Centaurs, Kuiper Belt Objects, etc.) retain information on their formation in their internal structure, surface appearance, and potential disruption behavior. In particular, the bodies' strength and morphology can reveal major population trends, such as spin rates, porosity, size distributions, ambient dust environment, etc. (e.g. Sánchez and Scheeres, 2014).

Space missions (Fujiwara et al., 2006; Lauretta et al., 2019; Watanabe et al., 2019) and ground-based observations (e.g. Busch et al., 2011) have shown that many smaller asteroids are loose collections of rubble, so-called rubble piles, rather than solid bodies. There is an abundance of evidence that nearly every object in the size range ~200 m to ~1 km is bound primarily by self-gravity, with significant void space or bulk porosity between irregularly shaped constituent particles (Walsh, 2018). The understanding of this population is derived from wide-ranging studies of shape and spin, decades of observational studies in numerous wavelengths (Pravec et al., 2006), and the in situ study of a few objects via spacecraft flyby or rendezvous (Fujiwara et al., 2006; Lauretta et al., 2019; Watanabe et al., 2019).

For this reason, in recent years, a consistent analytical and numerical effort has been carried out to better understand how large aggregates of irregular grains behave under stresses induced by compression (e.g. gravity), tension (e.g. centrifugal forces), and shear (e.g. seismic vibration). Works by Holsapple (2001, 2004, 2007) and Sharma (2013) introduce the application of continuum mechanics (angle of internal friction, bulk cohesion, e.g. Drucker and Prager, 1952) to the study of rubble pile asteroids. Sánchez and Scheeres (2014) study in more detail the notion of inter-grain cohesion and its effects on the bulk strength of these bodies. While these efforts have significantly increased our understanding of the morphology and behavior of small asteroids by comparing their results with observational data, they often lack laboratory measurements supporting their findings (Scheeres et al., 2010). In support of understanding how rubble piles behave and evolve, we have initiated a laboratory measurement campaign aimed at characterizing the mechanical properties of asteroid regolith.

One of the key parameters to understand rubble pile formation and evolution is their strength, in particular compressive and tensile strengths. Until recently, this king of strength information on the material composing primitive asteroids was mostly provided by measurements performed on meteorite falls, such as Tagish Lake, Orgueil, and Ivuna

* Corresponding author.
E-mail address: julie.brisset@ucf.edu (J. Brisset).

https://doi.org/10.1016/j.pss.2022.105533
Received 10 February 2022; Received in revised form 21 June 2022; Accepted 23 June 2022
Available online 30 June 2022

(see Ostrowski and Bryson, 2019, for a review). Compressive strengths of carbonaceous CI and CM meteorites range from 0.25 to 0.7 MPa for Tagish Lake (Brown et al., 2002) to 50 MPa for Murchison (Miura et al., 2008), and 82 MPa for Sutter Mills (Jenniskens et al., 2012). Tensile strengths are weaker at 0.8 MPa (Tagish Lake, Brown et al., 2002), 0.7 MPa (Ivuna, Tsuchiyama et al., 2008), and 2 MPa (**Murchison,** Miura et al., 2008). The recent spacecraft visit to rubble pile asteroids Ryugu and Bennu has allowed for a more detailed study of their boulders, and thus a better understanding of surface material in-situ. The analysis of craters on boulders on Bennu indicate an impact strength in the range 0.44–1.7 MPa (Ballouz et al., 2020). Thermal inertia data allows to constrain the tensile strength of boulders on Ryugu at 0.20–0.28 MPa (Grott et al., 2019). Both these numbers are on the very lower end of strengths measured from meteorites that have reached the surface of the Earth. This supports the idea of a sample bias towards stronger materials in the available primitive meteorite collection and the importance of in-situ measurements and targeted investigations on low-strength simulant materials for a thorough understanding of rubble-pile behavior.

In the present paper, we report of mechanical property measurements performed on granular samples with various grain sizes and with or without water ice frost surface coating. The samples used for measurements are composed of a high-fidelity asteroid regolith simulant (UCF/DSI–CI–2, Metzger et al., 2019), which has been shown to mimic the mechanical properties of CI Orgueil meteorite material, a carbonaceous chondrite, and is therefore representative of regolith found in primitive asteroids. Samples were prepared and measured at room-temperature and under cryogenic conditions (cooled to < 150 K using liquid nitrogen). The measurements performed include the strength of individual grains as well as bulk strengths in compression and shear. Our goal is to quantify the strength behavior of material composing small rubble-pile asteroids and here specifically, the role of the size and surface friction properties of the constituent grains.

In Section 2, we detail our measurement methods and we present measurement results in Section 3. In Section 4, we discuss our findings in the context of regolith and rubble pile characterization. Finally, we summarize our work in Section 5.

2. Measuring regolith strength

In order to characterize the influence of grain size and surface properties on the mechanical behavior of asteroid regolith, we chose to focus on three measurements:

- the angle of repose (AOR, Section 2.2.1). The AOR is the steepest angle of descent relative to the horizontal plane to which a material can be piled without further avalanching. It is an indicator of material bfshear strength in an unconfined configuration and can be used to determine inter-grain cohesion forces.
- the compression strength of the material (Section 2.2.2). By determining the relationship between stress (force per unit area) and strain (proportional deformation) in one-dimensional compression, we measure its Young Modulus (YM, Briaud, 2001). These measurements are performed in both confined and unconfined configurations.
- the shear strength of the material (Section 2.2.3). Here, the material is sheared while under normal stress in a confined configuration. The stress-strain curve reveals the shear yield point. The relationship between the shear yield stress and the normal stress at which it occurred allows for the measurement of the angle of internal friction (AIF), the bulk cohesion, and the tensile strength of the material (e.g., Perko et al., 2001). We note here that bulk cohesion is a property of the granular material and different from inter-grain cohesion forces.

The YM, AIF, and cohesion are material internal properties that fully characterize the response of a soil to stress. They can not be directly observed (e.g. from remote-sensing of a planetary surface) and have to be measured by applying stress to a soil sample or area. The AOR on the other hand can be measured by simple observations and is the only material property that can easily be detected at the surface of planetary bodies.

2.1. Regolith simulant samples

2.1.1. Preparation of granular samples

In order to prepare our regolith simulant samples, we aimed at reproducing the mechanical properties of actual asteroid regolith as closely as possible. To this purpose, we used the asteroid simulant from the Exolith Lab mimicking the CI Orgueil meteoritic composition (UCF/DSI–CI–2, Metzger et al., 2019), with a mineralogy based on the analysis by Bland et al. (2004). Metzger et al. (2019) performed a thorough analysis of this simulant using well-defined figures of merit comparing it to CI Orgueil (carbonaceous chondrite meteorite) material. Figures of merit included mineralogical composition, bulk density, and cobble mechanical strength. Their findings show that the UCF/DSI–CI–2 simulant is well-suited for reproducing bulk mechanical properties of granular samples of carbonaceous chondrite, and therefore, primitive asteroid material.

From experiments on simulated asteroid regolith (Brisset et al., 2018, 2020), we know that an important parameter in the behavior of granular material is the grain size distribution. The regolith grain size on asteroids and small bodies of the Solar System has been inferred both from thermal inertia measurements (Gundlach and Blum, 2013) and images returned from space missions (e.g. Hayabusa at Itokawa, Fujiwara et al. (2006), Hayabusa2 at Ryugu, Watanabe et al. (2019), OSIRIS-REx at Bennu, Lauretta et al. (2019)). Gundlach and Blum (2013) estimate grain sizes at the surface of about 20 asteroids ($<$100 km) and find they range from 0.1 to 10 mm. Spacecraft data also indicate grain sizes in this range, with the surfaces of Ryugu and Bennu being apparently depleted in fine (< 1 mm) grains (Sugita et al., 2019; Lauretta et al., 2019). We therefore chose to focus our study on grains in the size range 0.1–10 mm.

To this purpose, we prepared grains in three size distributions: fine grains, sieved to sizes < 600 μm; mm-sized, sieved to sizes between 1 and 6 mm; and cm-sized, sieved to sizes between 6 and 20 mm. The UCF/DSI–CI–2 simulant comes as a powder with an undefined particle size range < 1 mm. For fines, we simply sieved this powder to the target size distribution. In order to produce larger grains, this powder was mixed with water and prepared into cobbles of 10–20 cm in diameter. After drying for over 72h in a dehydrator, these cobbles were smashed into smaller grains, which were then sieved into mm- and cm-sized distributions.

2.1.2. Measurement conditions

In order to study the influence of grain surface properties on the behavior of the granular samples, we produced frosted grains in addition to our room-temperature (dry) samples. To this purpose, we prepared the samples in ambient air at cryogenic temperatures (< 150 K). These temperatures were achieved using liquid nitrogen baths, with which the sample materials never had direct contact.

The humidity in ambient air led to a layer of water frost at the surface of the grains. In order to determine the amount of frost/water ice present in the sample when prepared in this manner, we performed careful comparison of sample density with room-temperature samples. We measured an overall volumetric percentage of water ice of 5% within the air-prepared cryogenic samples. Cryogenic samples were cooled during the entire time of measurement, so that their surface properties remained the same during compression and shearing. This was performed by running an LN2 line into the vacuum chamber and around a copper block in which the sample cup was fitted.

2.1.3. Sample characterization

Grain size distribution By analyzing images of grain populations, we have measured the size distributions of our three sample types (fines, mm, cm, Fig. 1). Our fines consist mostly of grains around 250 μm in

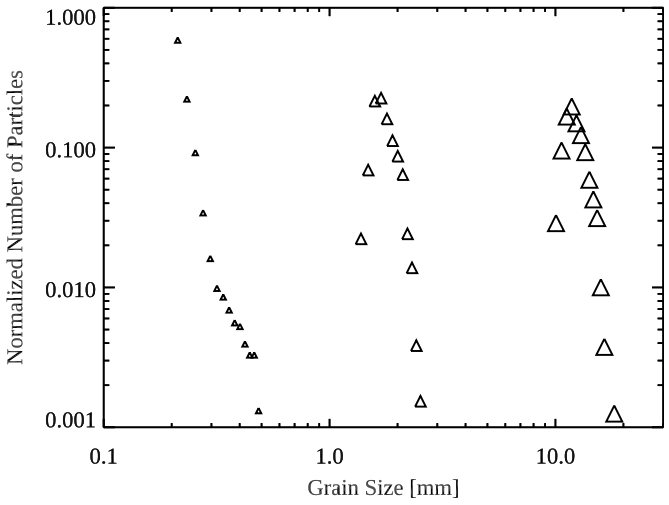

Fig. 1. Normalized grain size distribution for the three types of samples prepared: fines (sieved to < 600 μm); mm (sieved between 1 and 6 mm); and cm (> 1 cm).

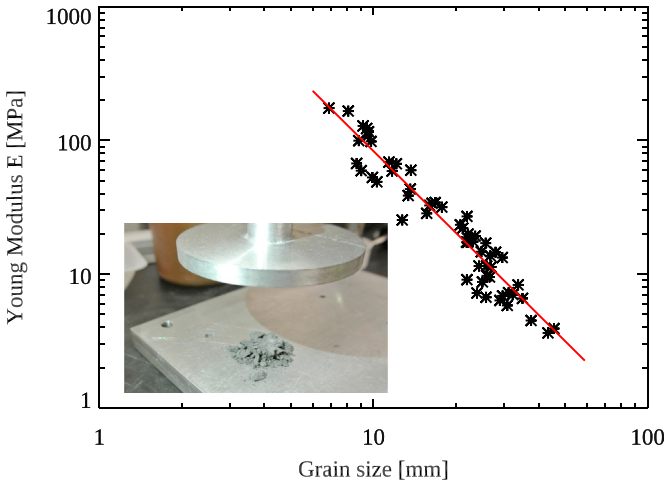

Fig. 2. Young Modulus of individual grains with sizes ranging from 8 to 50 mm. The inset shows a crushed grain using our compression setup. The force gauge plate that can be seen at the top is 5 cm in diameter and the crushed grain was about 1 cm in size. We find that $E \propto d^{-2}$, with E the grain Young Modulus and d its size (red line).

diameter, with a distribution tail towards 600 μm. Coarse grain samples have normal distributions peaking at 1.8 mm and 12 mm. An example of cm-sized grains can be seen in Fig. 3. The grains have irregular shapes resulting from the smashing during production, with rough surfaces.

Grain density and porosity We measured the average grain density using mass and volume measurements for 30 grains of the mm- and cm-size ranges. The mass was measured with a precision laboratory scale and the grain volume was measured using the 3D acquisition and volume computation of a Kinect sensor. This volume measurement was not possible for the finest grains, which were too small for the sensor acquisition. Given the small grain sizes in this range, we assumed grain densities were identical to the ones measured for the original simulant material (2.74 ± 0.01 g/cm^3, Metzger et al., 2019).

For the larger mm- and cm-sized grains, we obtained an average density of 1.61 ± 0.09 g/cm^3. Given a simulant material density of 2.74 ± 0.01 g/cm^3 (the constituent material we use to prepare our grains), this yields grain porosities around 41% for mm and cm samples. This is larger than the usually measured porosities of ~35% for CI meteorites (Ostrowski and Bryson, 2019). However, it is in range with one of the models considered by Grott et al. (2019) based on in-situ measurements of thermal inertia of boulders on rubble pile asteroid Ryugu.

Grain strength As the individual strength of grains plays an important role in the bulk behavior of the granular material, we have used our compression setup to measure the Young Modulus of a number of grains in the mm to cm range. The grains measured for strength ranged from 8 to 50 mm. We find that grains in this size range have decreasing strength with increasing grain size scaling approximately as $E \propto d^{-2}$, with E the grain Young Modulus and d its size.

Sample bulk properties Sample preparation for measurements consisted in loosely pouring grains into the sample container. Mass and volume measurements on over 30 samples prepared in this way showed that bulk porosities were at 35% for fines, and 63 and 65% for mm and cm samples, respectively. Given the microporosity of our mm and cm grains, we deduced a macroporosity of these samples of 37% and 41%, respectively. Frosted samples had porosities of 81%, 82%, and 83% for fines, mm, and cm samples, respectively, resulting in macroporosities of 67% and 69% for mm and cm samples, respectively.

2.2. Measurement techniques

2.2.1. Angle of repose measurements

In order to perform AOR measurements, we manually created piles of the various regolith samples studied. This was performed by filling a quasi-cylindrical container with the sample, maintaining it sealed. The container was then placed upside down on a flat surface and lifted in a regular, slow motion; the released sample material avalanched in a pile, which slope at rest is the AOR (Fig. 3).

For fines, the used container had a volume of about 500 mL (18 oz). For mm and cm samples, a 7.6 L (2 gallons) bucket was used.

For frosted samples, all contact surfaces (sample container and pouring surface) were kept at cryogenic temperatures using LN2 baths. The pouring happened on a short timescale in air saturated with cold N_2 gas from the evaporating LN2 bath of the pouring surface. In this way, the surface frosting was preserved during AOR measurements on frosted samples.

2.2.2. Compression strength measurements

In order to measure the Young Modulus of our simulated asteroid regolith, we designed a compression strength measurement setup allowing for both confined and unconfined measurements. The concept of this setup was to place a regolith sample into a container and lower a

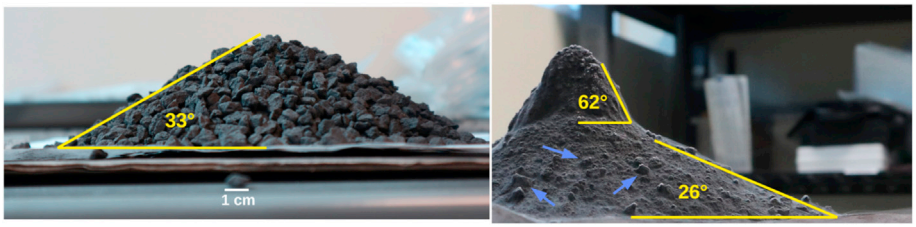

Fig. 3. AOR measurements: (left) Example of an angle of repose measurement performed on a pile of cm-sized grains. (right) Frosted fine grains (~0.1 mm) heap produced for angle of repose measurements. Blue arrows indicate some of the larger aggregates formed during heap pouring.

force gauge onto it using a precision stepper motor. The measurement started when the force gauge plate experienced its first contact with the sample surface and stoped when the sample resistance exceeded the torque produced by the stepper motor. This measurement included the strain of the sample from first contact to first yield and was used to measure the Young Modulus.

The sample container we used for confined compression measurements was a cylinder with an inner diameter of 50.8 mm and an inner height of 95.5 mm. The inner diameter corresponded to the diameter of the force gauge plate (50 mm), with a small gap allowing for frictionless motion of the gauge plate along the cylinder.

For unconfined measurements, we used a rectangular box as sample container with inner dimensions 150 × 136 × 100 mm, allowing for at least ten granular particle diameters in each dimension. For the largest grains (about 12 mm diameter), these dimensions allowed for a distance of at least four grain diameters from the outer edge of the gauge plate to the side of the container.

According to soil mechanics theory (Whitman, 1970), the response of granular samples to compression is not linear as expected from elastic materials. In Fig. 4, we show a typical response profile for such samples. In our compression measurement setup, we achieve compression stresses up to 0.03 MPa. As seen in Fig. 2, this is lower than the strength of individual grains. We therefore expect our sample's compression responses to show elastic, re-arrangement, and hardening behavior.

Given this overall non-linear response, the Young Modulus of the material depends on the applied stress and several characteristic values can be defined. For the purpose of the present work, we fit a function of the type $\sigma = A\varepsilon^B$ to our data, where σ is the stress in Pa applied to our samples and ε its strain (dimensionless). In the case of a sample in the elastic phase, $B = 1$ and the Young Modulus is a constant (A). If other phases are reached (grain re-arrangements and hardening), $B > 1$ and the Young Modulus is expressed as $E = AB\varepsilon^{B-1}$ as a function of the strain and $E = A^{1/B}B\sigma^{1-1/B}$ as a function of the stress. As the sample size is difficult to define for asteroid surface applications, it is more relevant to use the latter relationship to define a characteristic value for E. Here, we choose E_{1MPa} (the value of E when $\sigma = 1$ MPa) as a characteristic parameter, which will allow us to compare the strength between our various samples:

$$E_{1MPa} = A^{1/B}B(10^6)^{1-1/B} \tag{1}$$

Following Briaud (2001), we also define the tangent and secant Young Moduli, E_t and E_s, respectively, at a specific sample strain in order to compare our measurements with Earth sands and clays. We choose that strain to be 0.3 following common practice to measure these values at 30% of the peak strain (Briaud, 2001):

$$E_t = AB(0.3)^{B-1}$$
$$E_s = \frac{A}{0.3}(0.3)^B \tag{2}$$

2.2.3. Shear strength measurements

In order to produce shear stress-strain curves for the studied materials, we built a shear strength measurement setup. The regolith sample was placed in a container, which was split in its middle height. Both halves had the same dimensions of L89 × W89 × H57 mm. The bottom half of the container could be moved along a frictionless rail using a precision linear actuator to induce shear on the sample. The interface between the top and bottom of the container was designed for minimal friction. A normal force was applied to the top of the sample using a metal lid of the dimensions of the container crosssection and varying weights. During the shear motion of the bottom half of the container, the induced drag force on the top half was measured via a force gauge. Stress measurements on the empty setup showed friction levels that can be neglected compared to sample shear characteristics.

The measurement was started when the two sample container halves were aligned and ended when the bottom container half had moved all the way along the 150 mm rail. Such a measurement always included the point of shear yield of the sample, which was recorded to build the normal to shear yield stress curve, thus allowing for the measurement of the angle of internal friction (AIF) and bulk cohesion (C) of the material (Fig. 5). From these two quantities, the material tensile strength (T_s) was deduced: $T_s = C/\tan(\text{AIF})$.

2.2.4. Measurement errors

In order to evaluate error values for our measurements, we performed three measurements for each data point presented and averaged the values. For compressive strength, this led to a total of 12 measurements for sample grain type (3 measurement for each confined/unconfined and dry/frosted). For shear strength, this led to a total of 36 measurements for each grain type (3 measurements for 6 normal stresses for dry/frosted samples).

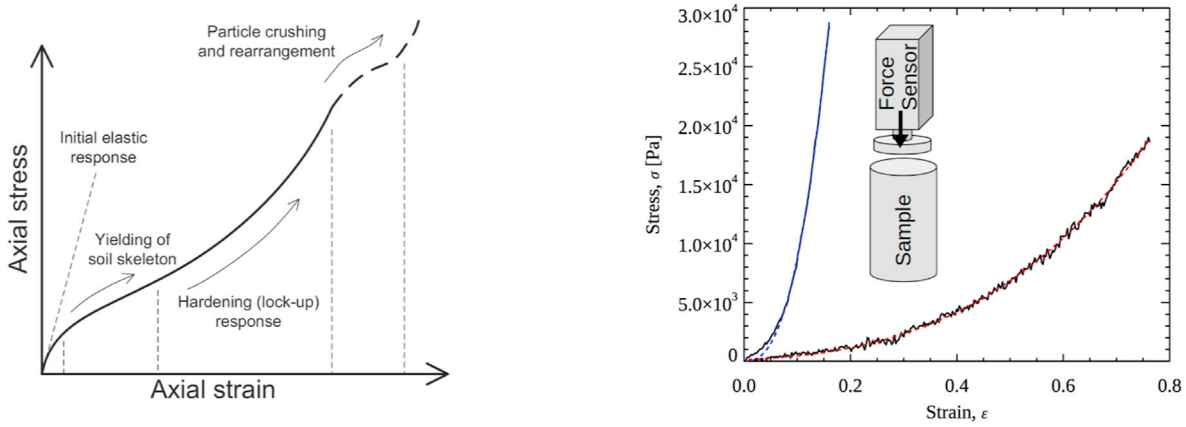

Fig. 4. Compression measurements: (left) Granular material response profile to compression (Whitman, 1970; Omidvar et al., 2012). For very low stresses, the stress-strain response corresponds to the elastic deformation of individual grains. When the compression force is higher than the friction force between grains, these start to slip against each other and the granular material yields due to structural re-arrangement. As the grains re-arrange and the granular structure compacts, the soil becomes stronger leading to a hardening "lock-up" response. Finally, the stress in the material is strong enough to break individual grains. (right) Measured stress-strain curve examples and their associated exponential fit (dashed curves) for fines frosted samples, confined (blue fit) and unconfined (red fit). The inset shows a schematic of the compression measurement setup for confined samples.

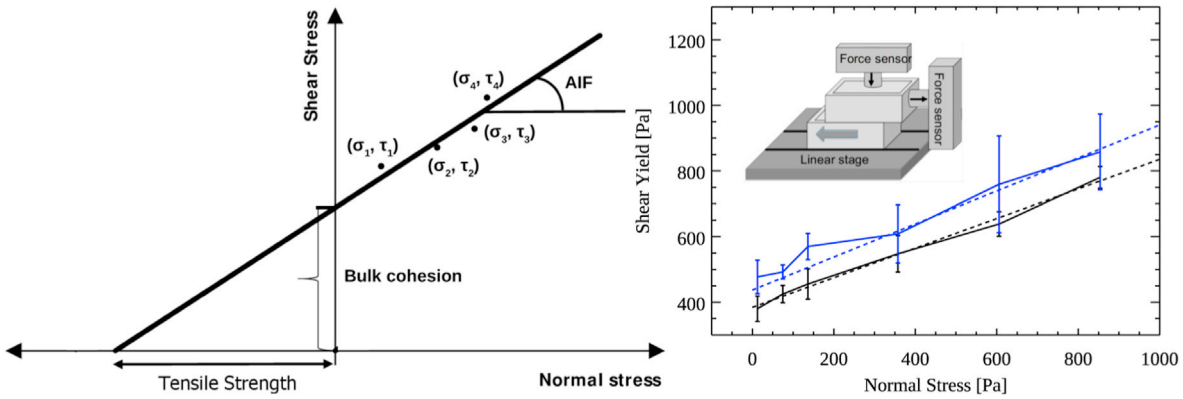

Fig. 5. Shear measurements: (left) Schematic of shear strength measurements, showing hypothetical data points (black dots) and the data fits yielding measurements (lines). Normal (σ) and shear (τ) stress are measured in Pascal. The angle of internal friction (AIF) is measured as indicated. The bulk cohesion is the intersection of the data fit with zero normal stress. The tensile strength of the material is measured as the intersection of the data fit with zero shear stress. (right) Mohr-Coulomb diagram providing the shear yield as a function of normal stress for fines at room (black) and cryogenic (blue) temperature. Dashed lines are linear fits to the data. The linear fits yield a material bulk cohesion of 384 ± 8 and 437 ± 39 Pa and an angle of internal friction of 24.2 ± 1.1 and 26.6 ± 3.4° for dry and frosted samples, respectively. The inset shows a schematic of the shear measurement setup.

3. Measurement results

3.1. Angle of repose

Table 1 lists the AOR measurements we obtained. The frosted fines presented two slopes as shown in Fig. 3. Explanations for this behavior include a difference in temperature induced by the pouring of the material in an ambient atmosphere (outer layers can warm up, frost can sublimate) or the formation of larger aggregates composed of the fine grain material, thus changing its granular behavior (such larger aggregates can be seen in the bottom part of the heap in Fig. 3, right). The formation of larger aggregates from powders during granular flow was also observed by Durda et al. (2014). As mentioned by Metcalf (1966), the notion of AOR becomes meaningless if the pile crushes under its own weight. In that case, the failed sides of the slope are not representative of the AOR properties of the material, but rather the still intact part of the pile.

As expected, we recognize a trend of decreasing angles of repose with increasing grain size for dry and frosted samples. The angles of repose of frosted samples for 0.1 and 1 mm-sized grains are higher than for same grains at room temperature, which is diagnostic of increased inter-grain cohesion forces. For cm samples, the difference between the dry and frosted samples is not noticeable, indicating that surface frost is not increasing the inter-grain forces enough for these large grains to compete with the grain weight.

The crumbled base of fine, frosted grain heaps has an angle of repose similar to the values for cm samples, which could support the idea of the tendency that the material has to form large aggregates when frosted due to increased inter-grain cohesion. Such large aggregates would temporarily dictate the flow behavior of the material until they partially dissolve again into fine grains (Rognon et al., 2008).

3.2. Compression strength

In Fig. 4, we show an example of our compression measurements for the fines frosted samples in confined and unconfined configurations. As described in Section 2.2.2, we observe the yielding and hardening phases of compression of the sample. The associated exponential fits are $\sigma = 3.0 \times 10^6 \varepsilon^{2.5}$ and $\sigma = 2.1 \times 10^4 \varepsilon^{3.2}$ for the confined and unconfined sample, respectively.

Based on the exponential fitting parameters on all the samples measured, we calculated the characteristic Young Moduli described above using Equations (1) and (2). The resulting values are listed in Table 2.

We can see that, for the same normal stress, frosted samples are stiffer than dry ones, more so in unconfined measurements than in confined ones. In addition, the grain size of the sample seems to not have a large influence on the sample stiffness in unconfined measurements. In confined measurements on the other hand, the sample stiffness decreases with increasing grains size.

The tangential and secant Young Modulus values show that our samples are much more elastic than traditional sand gravel, for which typical E_s values are around 50–100 MPa (e.g., Poulos and Davis, 1980). Our samples have elasticities closer to very soft silt and clays (0.2–1 MPa), even for coarser grains (mm and cm).

If we transpose our compression data from stress-strain curves to void ratio (also called porosity factor) vs. normal stress (Fig. 6), we can make a direct comparison with measurements performed on returned Apollo and Luna samples (Carrier III et al., 1972; Leonovich et al., 1977; Slyuta, 2014). We find that void ratios are overall higher than for the

Table 1
List of angles of repose for dry and frosted samples. For fine, frosted grains, we list both values measured as shown in Fig. 3.

Grain size	Average AOR dry [°]	Average AOR C [°]
fines	32.4 ± 3.3	44.0 ± 12.2/25.0 ± 1.8
mm	26.5 ± 1.8	34.1 ± 7.8
cm	24.3 ± 2.0	25.0 ± 0.8

Table 2
List of Young Moduli in MPa defined in Section 2.2.2 for all samples considered.

Sample	Dry			Frosted		
	E_{1MPa}	E_t	E_s	E_{1MPa}	E_t	E_s
Confined						
fines	1.400 ±0.22	0.204 ±0.003	0.094 ±0.001	1.860 ±0.039	0.549 ±0.025	0.279 ±0.013
mm	0.614 ±0.011	0.414 ±0.008	0.343 ±0.008	0.840 ±0.029	0.368 ±0.007	0.250 ±0.006
cm	0.317 ±0.012	0.187 ±0.007	0.155 ±0.008	0.532 ±0.022	0.332 ±0.011	0.270 ±0.013
Unconfined						
fines	0.243 ±0.011	0.046 ±0.002	0.030 ±0.001	0.754 ±0.145	0.039 ±0.007	0.017 ±0.003
mm	0.198 ±2.65 × 10^{-4}	0.090 ±0.001	0.072 ±9.86 × 10^{-4}	0.492 ±0.005	0.231 ±0.012	0.172 ±0.009
cm	0.326 ±0.008	0.163 ±0.002	0.129 ±0.003	0.791 ±0.094	0.190 ±0.004	0.110 ±0.003

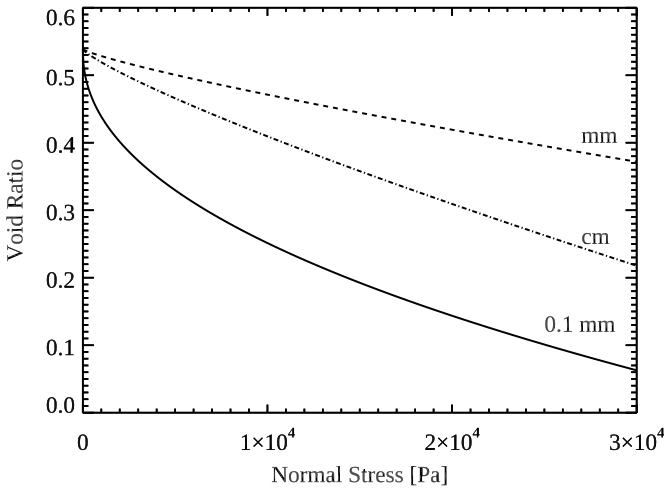

Fig. 6. Sample compressibility expressed using the void ratio $e = \frac{\varphi}{1-\varphi}$, φ being the porosity, for the dry samples.

measurements performed on Lunar soil and we get higher compressibility coefficients around 0.5 for fines and up to 0.6 for cm gains, compared to 0.2 (Apollo) and 0.3 (Luna). This indicates that asteroid regolith is more compressible than Lunar soil, which is of interest for the calibration of potential future penetrometry instruments for small bodies.

3.3. Angle of internal friction, cohesion, and tensile strength

In Fig. 5, we show an example of shear strength measurements on fine grains. Measurements display the linear behavior expected from the Mohr-Coulomb theory allowing for the computation of the material bulk cohesion, angle of internal friction, and tensile strength.

The bulk material cohesion and AIF obtained from the data linear fits are listed in Table 3. The general trend of the data is an increase in bulk cohesion and AIF for increasing grain sizes. This behavior was also observed by Shi et al. (2018) for grain sizes larger than about 250 μm.

The bulk cohesion is increased by about 50–70 Pa by the presence of frost on the grains in fines and mm samples. The AIF is higher for cryogenic samples by about 2 (fines) to 5° (cm).

In Table 3, we also list the sample tensile strengths deduced from the shear measurements. As intuitively expected, the general trend for the tensile strength is to decrease for increasing grain sizes. We note that the influence of frost on the grains seems to affect the tensile strength only for the coarser grains (cm). We also note that our tensile strength measurements are in good agreement with independent flexural strength measurements (Avdellidou et al., 2020).

Table 3
Bulk cohesion and angle of internal friction (AIF) computed for our asteroid simulant samples from shear strength measurements. We also show the normal stress threshold for the linear fits performed on the cryogenic sample data (see text for details).

	Dry			Frosted		
	Cohesion [Pa]	AIF [°]	Ts [Pa]	Cohesion [Pa]	AIF [°]	Ts [Pa]
Fines	384 ± 8	24.2 ± 1.1	852 ± 54	437 ± 39	26.6 ± 3.4	869 ± 181
mm	487 ± 24	32.6 ± 2.9	763 ± 98	557 ± 51	36.5 ± 6.9	755 ± 193
cm	566 ± 12	38.0 ± 1.7	721 ± 43	568 ± 21	43.2 ± 3.4	605 ± 61

3.4. Friction and internal friction

In Fig. 7, we show the coefficient of internal friction ($\mu_i = \tan(\text{AIF})$) as a function of the coefficient of friction ($\mu = \tan(\text{AOR})$) for the dry and frosted samples we have investigated. We observe that these two coefficients, and therefore the corresponding angles AIF and AOR, are not equal, as is often assumed in numerical simulations. In addition, both coefficients have inverse behaviors, with higher internal friction corresponding to lower friction, so that even the assumption that AOR and AIF variations go hand in hand is not accurate.

We note that grains with the highest potential for strong interlocking (large, angular grains) are the ones with the smallest inter-grain cohesion to weight ratio (AOR). The inverse relationship between friction and internal friction we see in Fig. 7 could therefore be due to the irregular shapes of our simulant grains, a parameter that is often difficult to model in simulations.

4. Discussion

4.1. Asteroid interiors

4.1.1. Angle of internal friction

From recent missions to small asteroids in the near-Earth environment, we have gained great insight into the rubble-pile nature of these bodies. The Japanese mission Hayabusa sent back the first in-situ images of such a rubble-pile asteroid, Itokawa (Fujiwara et al., 2006). The more recent missions Hayabusa2 and OSIRIS-REx have greatly added to the available pool of data on rubble piles by visiting the asteroids Ryugu (Watanabe et al., 2019) and Bennu (Lauretta et al., 2019), respectively. All three asteroids have in common that they are to a large extent covered by coarse, rugged boulders with sizes from centimeters to meters (Walsh et al., 2019; DellaGiustina et al., 2019; Sugita et al., 2019; Miyamoto et al., 2007). Fine dust is generally rare and absent on large fractions of their surfaces (Cambioni et al., 2021). However, so far, it has not been possible to probe the interiors of these asteroids although density measurements indicate high macro-porosities (Britt et al., 2003). From observation data coupled with numerical simulations, it seems like most C-type asteroids have internal friction in the range of 40° (Holsapple, 2001; Walsh, 2018). For fines, we measure friction angles around 25°. Only for coarse grains does interlocking allow for higher internal friction in the range of 40°. This indicates that the interior of rubble-pile asteroids is composed of coarse grains with probable size ranges > cm.

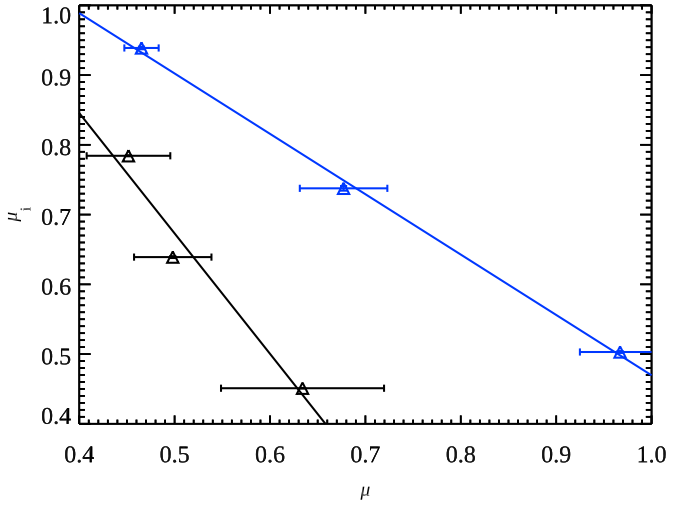

Fig. 7. Coefficient of internal friction $\mu_i = \tan(\text{AIF})$ as a function of the coefficient of friction $\mu = \tan(\text{AOR})$ (triangles). The solid lines show power-law fits yielding indices of −1.6 for dry (black) and −0.8 for frosted (blue) samples. AIF error bars are in the 10^{-3} - 10^{-4} range and thus smaller than the symbol size.

4.1.2. Bulk cohesion

From the Small Carry-on Impactor (SCI) experiment performed by Haya-busa2 on the surface of Ryugu, Arakawa et al. (2020) deduce a very low material cohesive strength of < 1.3 Pa. In addition, they infer the presence of a putative regolith sublayer with a higher strength between 140 and 670 Pa. The laboratory measurements that apply to the regolith top and sublayers are the unconfined and confined ones, respectively. Hence our AOR measurements apply to the very surface of the regolith layer, while the sublayer is best represented by our shear measurements.

In confined shear, we measure strengths ranging from 380 to 570 Pa (Table 3). These numbers are in good agreement with the ones deduced for Ryugu's sublayer. Another bulk cohesion measurement was deduced by Rozitis et al. (2014), who find that the asteroid (29075) 1950 DA, a rubble pile of about 1 km in size, must have a cohesive strength to be able to spin at its current rate. Assuming an AIF of 40°, they calculate that the value of this strength must be at least 64 Pa (numerical work by Hirabayashi and Scheeres, 2014, finds values between 75 and 85 Pa). They also derive that the surface of (29075) 1950 DA is covered in grains with sizes smaller than 6 cm. Our cm laboratory samples, which do have an internal friction around 40°, show a cohesive strength that is about one order of magnitude larger (see Table 3), which is in line with the requirement to avoid rotational breakup of asteroid (29075) 1950 DA. This supports the idea that rubble piles composed of cm-sized grains have non-zero cohesion, which allows them to spin at higher rates than expected by cohesionless theory.

Our conclusion is that, if the asteroid has an internal structure composed of coarse grains, it can explain both the internal friction and cohesion derived for small rubble-pile asteroids.

4.2. Rubble pile surfaces

4.2.1. Boulder and pebble strength

There are currently two ways of learning about the strength of individual boulders and pebbles at the surface of small asteroids: the laboratory analysis of meteoritic material, and the in-situ observation of rubble pile surfaces (soon to be complemented by the laboratory analysis of returned samples). The recently visited asteroids Bennu and Ryugu both present material at their surfaces that resembles CI/CM meteorites (Jaumann et al., 2019; Hamilton et al., 2020). Ryugu in-situ thermal inertia measurements reveal possible pebble and boulder porosities ranging from 41% to 55% with tensile strengths from 0.20 to 0.28 MPa (Grott et al., 2019). On Bennu, impact craters on boulders also indicate low impact strengths ranging from 0.44 to 1.7 MPa (Ballouz et al., 2020).

On the other hand, CI/CM meteorite porosity is measured at 35%/25%, respectively (Ostrowski and Bryson, 2019). Tensile strength measurements are measured to be a few factors up to an order of magnitude larger than in-situ data (0.8 MPa for Tagish Lake, 2 MPa for Murchison, and 2.8 MPa for Orgueil, see review in Ostrowski and Bryson, 2019). Their compressive strength is often several orders of magnitudes larger (50 MPa for Murchison, 82 MPa for Sutter Mills, and 98 MPa for La Criola, Ostrowski and Bryson, 2019), except for one, the Tagish Lake meteorite, which displays a compressive strength between 0.25 and 0.7 MPa (Brown et al., 2002).

In comparison, the CI simulant pebbles we produced in our investigation have a porosity around 41% (in good agreement with in-situ measurements) and a compressive strength dependent of their size, with values of a few MPa for 5 cm sized pebbles (Fig. 2, within the range of in-situ measurements). While we did not measure the tensile strength of individual grains, our bulk measurements (Table 3) are within the range of in-situ measurements determined from thermal inertia data. Overall, the meachnical behavior of our simulant material is in good agreement with in-situ data provided by the Hayabusa2 and OSIRIS-REx spacecraft at Ryugu and Bennu and indicates that the meteorite collection available to us is biased towards more compact, stronger samples, the only ones able to survive traveling through the atmosphere.

4.2.2. Surface strength

From our unconfined measurements, we can infer properties of surface material on small rubble pile asteroids. In order to deduce a surface cohesive strength from our AOR measurements, we worked with an equation used in numerical simulations of rubble-pile asteroids (Sánchez and Scheeres, 2016; 2018). There, the material's cohesive strength is calculated using

$$\sigma_c = \sigma_{yy} \frac{ff \cos 45^\circ}{\sqrt{3}} \tan \theta \tag{3}$$

where σ_{yy} is the tensile strength of the contact between two particles, ff is the filling fraction (1-porosity) and θ is the AIF (See C for details). If we apply these simulations to reproducing the AORs we measure experimentally, we find that $\sigma_{yy} = 75$ Pa for dry samples. Using this number and our measured values for the AIF (θ), we find that our dry mm and cm sample piles have a cohesive strength of 5 and 11 Pa, respectively. These values are a factor 3 to 10 larger than the one deduced for Ryugu's surface material.

4.2.3. Surface activity

Numerical calculations by Hirabayashi et al. (2015) show that the difference in strength in regolith between a weaker top layer and a stronger sublayer can lead to surface mass shedding in small bodies that approach their disruption limit due to rapid rotation. Such a mass shedding is then observed as surface activity. In such a configuration, mass shedding occurs due to shear failure of the surface material in the equatorial region, where the equivalent gravity is very low.

From the cohesion obtained combining our measurements with numerical simulations (Equation C.9 above), we see that such cohesion differences can arise from grain size differences, with larger grains being more cohesive, as well as from a difference in surface properties of grains. This means that strength differences between the top layers of a small, fast-rotating rubble pile can arise from a difference in grain size distribution between them (e.g. fine grain depletion at the surface due to solar wind exposure, Housen and Wilkening, 1982). Here, surface activity would be a symptom of the presence of a fine grain population in sublayers of the asteroid. Similarly, the continued presence of water ice in the core of an asteroid (Schorghofer, 2008) would result in a sublayer of frosted grains having a higher strength than the dry top layer where any water ice would have long sublimated at the solar distances common asteroids are found. In this configuration, surface activity would be an indicator of the presence of water ice inside the asteroid, while no water ice is present (and therefore, detected) at the surface.

The examples above show how surface modification due to exposure to space weathering compared to a more pristine interior could lead to a mechanism for regular shedding events. After each shedding event, new grain layers are exposed to space weathering, either loosing their fine grain fraction or changing their surface properties over the time they are exposed. Eventually, these new top layers experience changes in cohesive strength compared to their sublayers and a new shedding event takes place.

Our work also shows that even a single layer of same-sized coarse grains can experience strength differences with the depth to the surface. Indeed, confined shear measurements show that large, cm-sized grains make for a stronger material than smaller grains due to interlocking. However, these same large grains make for a weaker material in unconfined conditions (AOR) compared to smaller grains due to their weight overpowering inter-particle forces. As the material strength behavior is reversed from the confined sublayers to the unconfined surface, the depth at which interlocking becomes a relevant strength mechanism reprensents a transition between stronger and weaker behavior for the same population of grains. In this case, the rubble pile would behave like a body with a more cohesive core, despite the fact that the properties of individual grains would be the same between the surface and sublayers.

When simulating the spinup disruption of rubble-pile asteroids, Walsh et al. (2012) find a similar result: for granular material with large angles of internal friction around 40°, they find a disruption pattern of mass shedding rather than global failure as seen for materials with lower internal friction ($\sim 20°$). While this behavior might be enhanced by the assumed crystalline packing of the material (Hirabayashi et al., 2015), the interlocking of grains in the confined parts of the simulated asteroid could contribute to its enhanced internal strength and therefore its surface shedding behavior. This supports the thought that, if a rubble-pile asteroid was composed of a population of coarse irregular grains of about the same size, it would naturally disrupt by shedding surface mass due to the material strength difference between the confined core and the unconfined surface.

5. Summary and conclusion

In this paper, we present the laboratory measurement of bulk mechanical properties of asteroid simulant granular samples. The samples were prepared from a high-fidelity regolith simulant and included three grain size distributions as well as frost-coated grains. Measurements performed include angles of repose, compression, and shear strength, yielding the bulk quantities of Young Modulus, angle of internal friction, bulk cohesion, and tensile strength. Our findings can be summarized as follows:

- All measurements (except for unconfined compression) show a clear dependence on the grain size in the granular sample. In compression, coarser grains display a weaker stress response than finer grains. This trend is reversed in shear measurements, with cm samples being stronger than fines, due to the interlocking of irregular shapes grains. The tensile strength decreases with increasing grain size (as expected).
- All measurements show stronger samples when frost-coated. In compression, frosted samples are about one order of magnitude stronger than dry ones (comparing stress measurements for a same strain, see Fig. 4). In shear the strength was about 1.5 times higher for frosted samples than for dry ones (Fig. 5).

In conclusion, we observe that fine grains are stronger than large ones in compression, but weaker in shear, where grain interlocking is the dominant source of strength (Shi et al., 2018). The increase in inter-grain cohesion through a change in surface properties consistently strenthen the samples in both compression and shear. We conclude that surface modification processes, such as grain-size sorting, fine grain depletion, or dessication can be factors of strength differences between regolith layers on small asteroids. Furthermore, even a monodisperse population of irregularly-shaped grains can show strength differences with differences in confinement, i.e. regolith sublayers behaving differently than the surface. As shown by Hirabayashi et al. (2015), a weaker surface layer on top of a stronger sublayer could be at the origin of surface mass shedding on rotating asteroids. Our laboratory study indicates that such strength differences can easily be achieved in rubble-pile asteroids composed of similarly-sized coarser grains.

Author statement

Julie Brisset: Conceptualization, Methodology, Formal Analysis, Investigation, Resources, Data Curation, Writing – Original Draft, Writing – Review & Editing, Visualization, Supervision, Project Administration, Funding Acquisition. Paul Sánchez: Conceptualization, Methodology, Formal Analysis, Investigation, Writing – Original Draft, Visualization. Christopher Cox: Formal Analysis, Investigation, Data Curation, Visualization, Supervision. Dennis Corraliza: Investigation. John Hatchitt: Investigation. Alexander Madison: Investigation. Thomas Miletich: Methodology, Formal Analysis, Investigation.

Declaration of competing interest

The authors declare the following financial interests/personal relationships which may be considered as potential competing interests: Julie Brisset reports financial support was provided by National Science Foundation.

Acknowledgement

This work was funded by the National Science Foundation, award \# 1830609.

Appendix AMeasurement Hardware

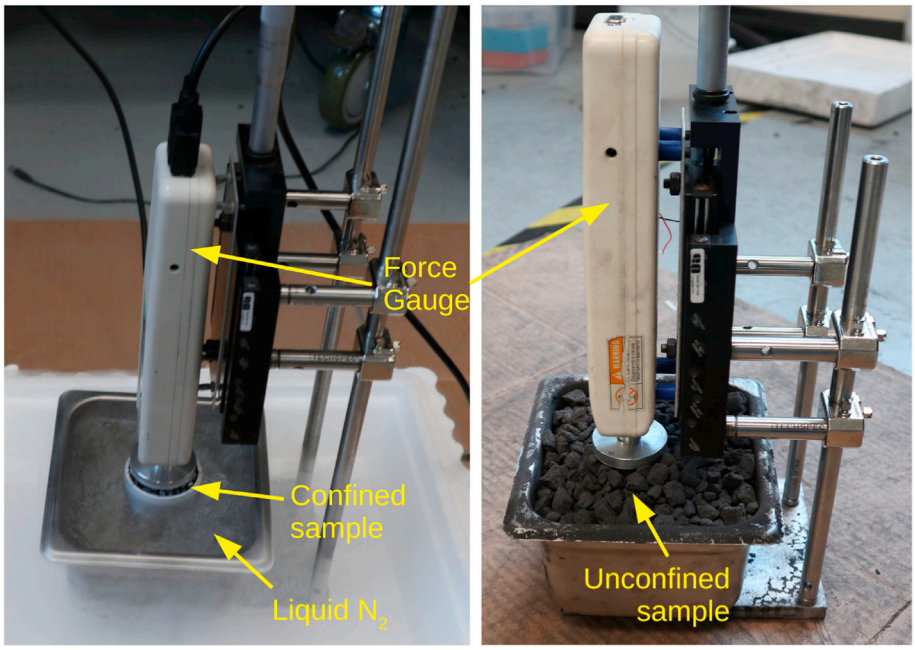

Fig. A.8. Compression strength measurement setup: a force gauge is lowered onto the granular sample using an optical stage and precision stepper motor. The gauge displacement and read resistance force are recorded to generate a stress-strain curve as seen in Fig. 4. (left) Example of a cryogenic measurement on a confined sample of mm-sized grains. (right) Example of a room temperature measurement on an unconfined sample of cm-sized grains.

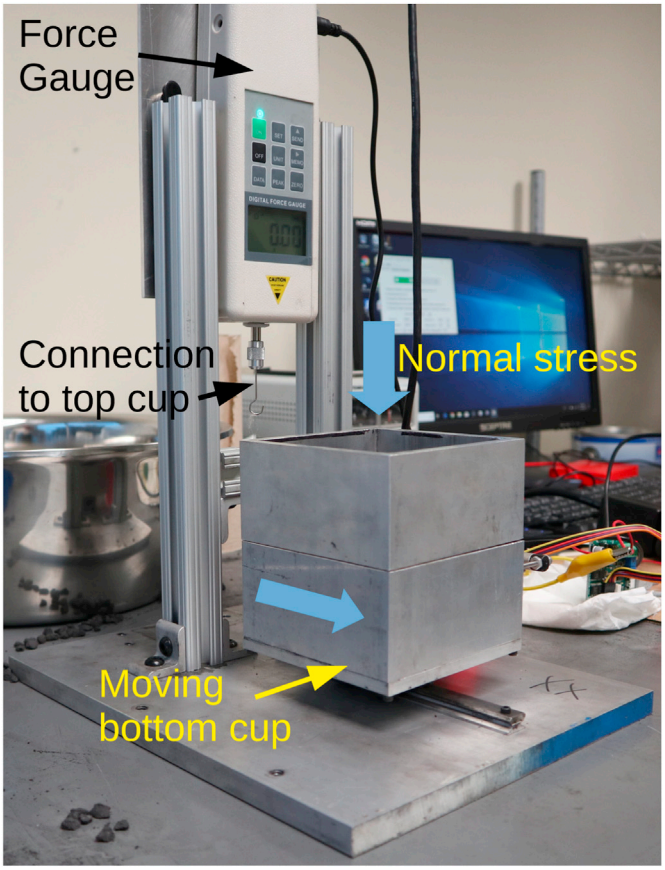

Fig. A9. Shear strenght measurement setup. The sample is placed into a shearable container, which bottom half can be moved using a precision stepper motor. A normal force is applied from the top using masses and a force gauge reads the resistance force of the top half of the sample container.

Appendix B. Compression Measurement Fitting Parameters

Table B4
Compression curve fitting parameters for exponential fits of the form $\sigma = A\varepsilon^B$, σ being the normal stress in the sample and ε the strain. 1/0 values for Cryogenic and Confined samples indicate Yes/No for the sample, respectively. σ_A and σ_B are the 1-σ fitting errors for each parameter.

Grain Size [mm]	Cryogenic	Confined	A	σ_A	B	σ_B
0.1	0	0	57256	13100.2	1.55	0.13
0.1	0	1	385663	27539.7	2.18	0.05
0.1	1	0	79250.2	60036.3	2.29	0.6
0.1	1	1	895191	202915	1.97	0.06
1	0	0	97859.3	6710.62	1.26	0
1	0	1	440936	39020.1	1.21	0.05
1	1	0	259471	69435.5	1.34	0.03
1	1	1	440120	39798.9	1.47	0.1
10	0	0	177991	12157.9	1.27	0.07
10	0	1	199024	36423.5	1.21	0.11
10	1	0	262735	12978.7	1.72	0.36
10	1	1	355959	55027.2	1.23	0.12

Appendix C. Numerical Simulation Details

Appendix C1. Simulation Code and Setup

The simulation program that is used for this research applies a Soft-Sphere Discrete Element Method (SSDEM) (Cundall, 1971; Cundall and Hart, 1992), implemented as a computational code (in house developed) to simulate a granular aggregate (Biswas et al., 2003; Sánchez and Scheeres, 2009; 2011, 2012). The particles, modelled as spheres that follow uniform size distribution between predetermined lower and upper limits, and interact through a soft-repulsive potential when in contact. This method considers that two particles are in contact when they overlap. When this happens, normal and tangential contact forces are calculated (Herrmann and Luding, 1998). The former is modelled by a hertzian spring-dashpot system and is always repulsive, keeping the particles apart; the latter is modelled with a linear spring that satisfies the local Coulomb yield criterion. The normal elastic force is modelled as

$$\vec{\mathbf{f}}_e = k_n \xi^{3/2} \hat{\mathbf{n}} \tag{C1}$$

the damping force as:

$$\vec{\mathbf{f}}_d = -\gamma_n \dot{\xi} \hat{\mathbf{n}}, \tag{C2}$$

and the cohesive force between the particles is calculated as

$$\vec{\mathbf{f}}_c = -2\pi \frac{r_1^2 r_2^2}{r_1^2 + r_2^2} \sigma_{yy} \hat{\mathbf{n}} \tag{C3}$$

where r_1 and r_2 are the radii of the two particles in contact, σ_{yy} is the tensile strength of this contact and $\hat{\mathbf{r}}_{12}$ is the branch vector between the centres of these two particles. The total normal force is calculated as $\vec{\mathbf{f}}_n = \vec{\mathbf{f}}_e + \vec{\mathbf{f}}_d$. In these equations, k_n is the elastic constant, ξ is the overlap of the particles, γ_n is the damping constant (related to the dashpot), $\dot{\xi}$ is the rate of deformation and $\hat{\mathbf{n}}$ is the vector joining the centres of the colliding particles. This dashpot models the energy dissipation that occurs during a real collision.

The tangential component of the contact force models surface friction statically and dynamically. This is calculated by placing a linear spring attached to both particles at the contact point at the beginning of the collision (Herrmann and Luding, 1998; Silbert et al., 2001) and by producing a restoring frictional force $\vec{\mathbf{f}}_t$. The magnitude of the elongation of this tangential spring is truncated in order to satisfy the local Coulomb yield criterion $|\vec{\mathbf{f}}_t| \leq \mu |\vec{\mathbf{f}}_n|$.

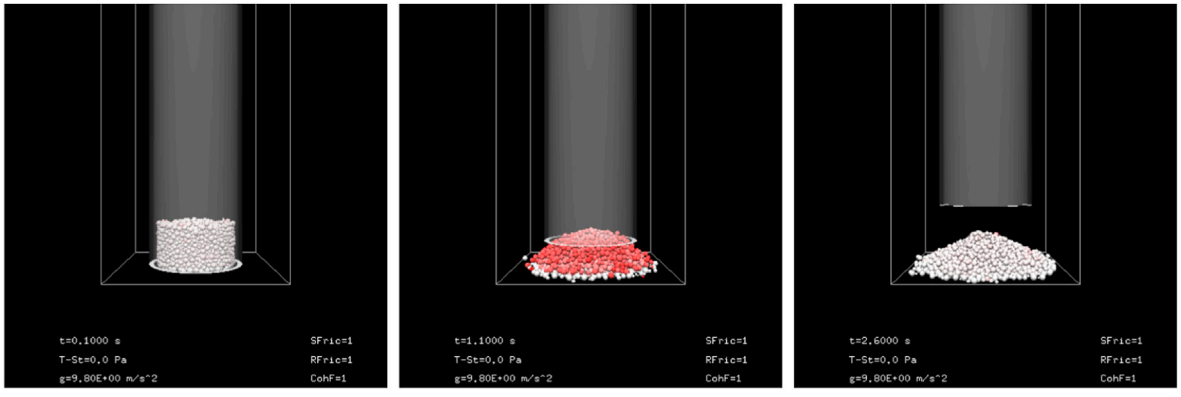

Fig. C10. Simulation of the formation of a granular pile with cohesionless, millimetre size particles. The slope angle is 28°. The redder the colour, the faster the particle is moving.

For this particular set of simulations, we have chosen to use material parameters experimentally measured so that simulations are as realistic as possible. The simulated particles are spherical grains with an element of rolling friction so that their behaviour mimics that of non-spherical particles. Rolling friction (Ai et al., 2011; Sánchez and Scheeres, 2016) has also been implemented in order to mimic the behavior of aggregates formed by non-spherical grains. Particles are subjected to a torque that opposes the relative rotation of any two particles in contact. This model "places" a winding spring of sorts that is extended when two contacting particles roll on one another along with a velocity dependent dashpot. Much like the tangential spring that models static friction between particles in our code, this spring also breaks and allows rotation when a certain limit has been reached. This torque, similar to surface-surface friction, is implemented as linearly dependent on the relative angular displacement of any two particles in contact and has a limiting value of:

$$M_r^m = \mu_r R_r |\vec{\mathbf{f}}_n| \tag{C4}$$

where μ_r is the coefficient of rolling resistance and $R_r = r_1 r_2/(r_1 + r_2)$ is the rolling radius.

The viscous damping torque M_r^d is assumed to be dependent on the relative rolling angular velocity $\dot{\theta}_r$ between the two particles in contact and the damping constant C_r:

$$M_{r,t+\Delta t}^d = \begin{cases} -C_r \dot{\theta}_r & \text{if } |M_{r,t+\Delta t}^k| < M_r^m \\ -f C_r \dot{\theta}_r & \text{if } |M_{r,t+\Delta t}^k| = M_r^m \end{cases} \tag{C5}$$

This last equation contains a term f, which determines whether the viscous damping torque is only active before the contact rolling torque is fully mobilised ($f = 0$) or if it is always present ($f = 1$). For simplicity we have chosen $f = 0$ for our simulations.

We use 5000 spherical grains for all simulations. There were two sets of simulations, the first with particles between 0.8 and 1.2 cm in size simulating cm samples; the second with particles between 1 and 6 mm in size, simulating mm samples. No simulations were carried out with sub-millimetre particles (fines) as that would take impractically long periods of time to finish. We used a density of 1610 kg m^{-3} (see Section 2.1.3), a Young Modulus of 5×10^7 N m^{-2} (see Fig. 2), and assumed Poisson ratio of 0.25. Based on these parameters, the values of k_n and γ_n can be calculated as:

$$k_n = \frac{2Y\sqrt{r_{eff}}}{3(1-\nu^2)} \tag{C6}$$

$$\gamma_n = A\sqrt{\xi} \tag{C7}$$

where R_{eff} is the effective radius of the colliding spheres of radii r_1 and r_2

$$\frac{1}{r_{eff}} = \frac{1}{r_1} + \frac{1}{r_2} \tag{C8}$$

The coefficient A, can be adjusted in order to manipulate the coefficient of restitution of the particles. For our simulations, this parameter was adjusted to obtain a coefficient of restitution of 0.3, which was the average coefficient of restitution measured experimentally. The chosen values were 2×10^{-4} and 2×10^{-5} for cm and mm particles, respectively.

The particles are contained inside a solid, frictionless cylinder that is allowed to move upwards so that the experiments to measure the slope angle of a granular pile can be reproduced. Initially, the particles are placed in a number of concentric circles parallel to the bottom of the cylinder. Once a disc grows enough to touch the walls of the cylinder, a second disc, parallel to the first and above it, is started. The procedure is continued until all the particles in the simulation have been given a position. After this, all the particles are provided with a small random velocity and then they are allowed to settle under a constant gravity of 9.8 m s^{-2}. When the particles have settled, the simulation starts and the cylinder is lifted with a speed of 2.5 cm s^{-1}. In order to provide a rough base for the formation of the pile, all the particles are set to be motionless upon contact with the bottom of the container. The simulation ends when all the particles have left the cylinder and a stable pile has been formed. Figure C10 shows snapshots of the simulation with mm particles at different stages of pile formation. The colour of the particles reflects their normalized speed and it changes from 0 (absolute white) to 1 (absolute red). The normalisation factor used is the potential energy of a particle of average size at the top of the arrangement before the cylinder starts moving.

Cylinders of 19 and 8 cm were used to contain the cm and mm particles respectively. The cylinder size was changed to avoid the use of an impractically large number of particles.

Appendix C2. Simulation Results

The objective of the simulations presented here is to determine the set of grain surface properties that lead to bulk material behaving as seen in laboratory measurements. As shown by Zhou et al. (2014), the angle of repose is mainly sensitive to the sliding and rolling friction coefficients between the particles. Therfore, we first assume that the inter-particle forces in dry conditions can be neglected compared to grain weight. We then determine the surface friction coefficients μ_s (sliding) and μ_r (rolling) for mm and cm grains that are able to reproduce the laboratory AORs. We find that the friction parameters summarized in Table C.5 are adequately reproducing laboratory AOR measurements for the case of cohesionless particles.

Table C5
Friction parameters for the simulations of the AOR of mm and cm samples. μ_s is the coefficient of sliding friction and μ_r of rotational friction.

	μ_s	μ_r	AOR
cm	0.5	0.5	26°
mm	0.5	0.9	28°

The parameters that the simulation code uses are related to real material characteristics and so, at least from a qualitative point of view, it seems that the shape of the grain is more important for mm grains than for cm ones even if their surface sliding friction is the same.

Having found that the simulation code could reproduce these initial findings, the next step was to find the cohesive strength needed to reproduce the angles of repose of the frosted samples. In order to do this, we specified a value for the tensile strength of the bonds between pairs of contacting particles as described in the previous section.

Simulations showed that for cm particles, a σ_{yy} of up to 75 Pa would not produce any noticeable change in the slope of the piles. Beyond this value, the piles would increase their slope. This means that, with the friction coefficients of Table C5, mm and cm grains can have inter-grain tensile strength of up to 75 Pa.

Given that experimentally the cm samples would not present a change in slope with frosting of the grains, we took this as an upper limit of the tensile strength for frosted cm samples. On the other hand, mm samples presented an increase in their angle of repose of 5° experimentally between dry and frosted conditions. This increment could be obtained in simulations with a σ_{yy} of ≈200 Pa.

The cohesive strength of these samples can then be calculated with the expression obtained by Sánchez and Scheeres (2016) and corrected in Sánchez and Scheeres (2018):

$$\sigma_c = \sigma_{yy} \frac{ff \cos 45^\circ}{\sqrt{3}} \tan \theta \tag{C.9}$$

where ff is the filling fraction (1-porosity) and θ is the AIF. We take the filling fraction to be 0.18 as per the frosted porosity values we measured in Section 2.1.3. The AIF values are taken from Table 3. With this, it is possible to calculate that the cohesive strength of the formed piles is 4.9 Pa and 10.9 Pa for piles formed by cm and mm samples, respectively. This increase in cohesion with a decrease in particle size is a similar relationship to the one found numerically for small asteroids, which could potentially explain their high rotation rates (Sánchez and Scheeres, 2014). We note that the increase in cohesive strength of the samples does not scale directly with the grain size, unlike what was seen in simulations of van der Waals (VdW) cohesive forces (Scheeres et al., 2010). This could have several reasons, including the irregular shapes of the experimental grains leading to irregular number of contacts between grains.

Indeed, one drawback of the simulations we have used here is that we have used perfectly spherical particles and real particles are not naturally spherical. In our simulations, we have used these particles for all simulations and so any pair of particles in contact can only have one contact. In the experiments, particles are very non-spherical, and so they can have multiple contacts. The change in the bonding force created by the frost will change with the effective area of contact, where frost bonds the particles and even though for spherical particles the important size scale for the bonding force is the particle size, for non-spherical particles, it is the effective contact area.

References

Ai, J., Chen, J.-F., Rotter, J.M., Ooi, J.Y., 2011. Assessment of rolling resistance models in discrete element simulations. Powder Technol. 206 (3), 269–282.

Arakawa, M., Saiki, T., Wada, K., Ogawa, K., Kadono, T., Shirai, K., Sawada, H., Ishibashi, K., Honda, R., Sakatani, N., et al., 2020. An artificial impact on the asteroid (162173) ryugu formed a crater in the gravity-dominated regime. Science 368 (6486), 67–71.

Avdellidou, C., Di Donna, A., Schultz, C., Harthong, B., Price, M.C., Peyroux, R., Britt, D., Cole, M., et al., 2020. Very weak carbonaceous asteroid simulants i: mechanical properties and response to hypervelocity impacts. Icarus 341, 113648.

Ballouz, R.-L., Walsh, K., Barnouin, O., DellaGiustina, D., Asad, M.A., Jawin, E., Daly, M., Bottke, W., Michel, P., Avdellidou, C., et al., 2020. Bennu's near-earth lifetime of 1.75 million years inferred from craters on its boulders. Nature 587 (7833), 205–209.

Biswas, P., Sanchez, P., Swift, M.R., King, P., 2003. Numerical simulations of air-driven granular separation. Phys. Rev. 68 (5), 050301.

Bland, P.A., Cressey, G., Menzies, O.N., 2004. Modal mineralogy of carbonaceous chondrites by x-ray diffraction and mössbauer spectroscopy. Meteoritics Planet Sci. 39 (1), 3–16.

Briaud, J.-L., 2001. Introduction to soil moduli. Geotech. News 19 (2), 54–58.

Brisset, J., Colwell, J., Dove, A., Abukhalil, S., Cox, C., Mohammed, N., 2018. Regolith behavior under asteroid-level gravity conditions: low-velocity impact experiments. Prog. Earth Planet. Sci. 5 (1), 73.

Brisset, J., Cox, C., Anderson, S., Hatchitt, J., Madison, A., Mendonca, M., Partida, A., Remie, D., 2020. Regolith Behavior under Asteroid-Level Gravity Conditions: Low-Velocity Impacts into Mm-And Cm-Sized Grain Targets arXiv preprint arXiv: 2008.08720.

Britt, D.T., Yeomans, D., Housen, K., Consolmagno, G., 2003. Asteroid Density, Porosity, and Structure.

Brown, P.G., Revelle, D.O., Tagliaferri, E., Hildebrand, A.R., 2002. An entry model for the tagish lake fireball using seismic, satellite and infrasound records. Meteoritics Planet Sci. 37 (5), 661–675.

Busch, M.W., Ostro, S.J., Benner, L.A., Brozovic, M., Giorgini, J.D., Jao, J.S., Scheeres, D.J., Magri, C., Nolan, M.C., Howell, E.S., et al., 2011. Radar observations and the shape of near-earth asteroid 2008 ev5. Icarus 212 (2), 649–660.

Cambioni, S., Delbo, M., Poggiali, G., Avdellidou, C., Ryan, A., Deshapriya, J., Asphaug, E., Ballouz, R.-L., Barucci, M., Bennett, C., et al., 2021. Fine-regolith production on asteroids controlled by rock porosity. Nature 598 (7879), 49–52.

Carrier III, W.D., Bromwell, L.G., Torrence Martin, R., 1972. Strength and compressibility of returned lunar soil. In: Lunar and Planetary Science Conference Proceedings, vol. 3, p. 3223.

Cundall, P.A., 1971. A computer model for simulating progressive, large-scale movement in blocky rock system. In: Proceedings of the International Symposium on Rock Mechanics, 1971.

Cundall, P.A., Hart, R.D., 1992. Numerical Modelling of Discontinua. Engineering Computations.

DellaGiustina, D., Emery, J., Golish, D., Rozitis, B., Bennett, C., Burke, K., Ballouz, R.-L., Becker, K., Christensen, P., d'Aubigny, C.D., et al., 2019. Properties of rubble-pile asteroid (101955) bennu from osiris-rex imaging and thermal analysis. Nat. Astron. 3 (4), 341–351.

Drucker, D.C., Prager, W., 1952. Soil mechanics and plastic analysis or limit design. Q. Appl. Math. 10 (2), 157–165.

Durda, D., Sanchez, P., Fischer, A., Devaud, G., Scheeres, D., Roark, S., Kaptchen, P., Dissly, R., 2014. The size distribution of boulders' formed during slope failure in piles of self-cohesive powders: application to the morphology of regoliths on small asteroids. In: Lunar and Planetary Science Conference, vol. 45, 2015.

Fujiwara, A., Kawaguchi, J., Yeomans, D., Abe, M., Mukai, T., Okada, T., Saito, J., Yano, H., Yoshikawa, M., Scheeres, D., et al., 2006. The rubble-pile asteroid itokawa as observed by hayabusa. Science 312 (5778), 1330–1334.

Grott, M., Knollenberg, J., Hamm, M., Ogawa, K., Jaumann, R., Otto, K.A., Delbo, M., Michel, P., Biele, J., Neumann, W., et al., 2019. Low thermal conductivity boulder with high porosity identified on c-type asteroid (162173) ryugu. Nat. Astron. 3 (11), 971–976.

Gundlach, B., Blum, J., 2013. A new method to determine the grain size of planetary regolith. Icarus 223 (1), 479–492.

Hamilton, V., Simon, A., Kaplan, H., Christensen, P., Reuter, D., DellaGiustina, D., Haberle, C., Hanna, R., Brucato, J., Praet, A., et al., 2020. Vnir and tir spectral characteristics of (101955) bennu from osiris-rex detailed survey and reconnaissance a observations. In: 51st Annual Lunar and Planetary Science Conference, p. 1049. No. 2326.

Herrmann, H., Luding, S., 1998. Modeling granular media on the computer. Continuum Mech. Therm. 10 (4), 189–231.

Hirabayashi, M., Sánchez, D.P., Scheeres, D.J., 2015. Internal structure of asteroids having surface shedding due to rotational instability. Astrophys. J. 808 (1), 63.
Hirabayashi, M., Scheeres, D.J., 2014. Stress and failure analysis of rapidly rotating asteroid (29075) 1950 da. Astrophys. J. Lett. 798 (1), L8.
Holsapple, K., 2001. Equilibrium configurations of solid cohesionless bodies. Icarus 154 (2), 432–448.
Holsapple, K.A., 2004. Equilibrium figures of spinning bodies with self-gravity. Icarus 172 (1), 272–303.
Holsapple, K.A., 2007. Spin limits of solar system bodies: from the small fast-rotators to 2003 el61. Icarus 187 (2), 500–509.
Housen, K.R., Wilkening, L.L., 1982. Regoliths on small bodies in the solar system. Annu. Rev. Earth Planet Sci. 10, 355–376.
Jaumann, R., Schmitz, N., Ho, T.-M., Schröder, S., Otto, K.A., Stephan, K., Elgner, S., Krohn, K., Preusker, F., Scholten, F., et al., 2019. Images from the surface of asteroid ryugu show rocks similar to carbonaceous chondrite meteorites. Science 365 (6455), 817–820.
Jenniskens, P., Fries, M.D., Yin, Q.-Z., Zolensky, M., Krot, A.N., Sandford, S.A., Sears, D., Beauford, R., Ebel, D.S., Friedrich, J.M., et al., 2012. Radar-enabled recovery of the sutter's mill meteorite, a carbonaceous chondrite regolith breccia. Science 338 (6114), 1583–1587.
Lauretta, D., DellaGiustina, D., Bennett, C., Golish, D., Becker, K., Balram-Knutson, S., Barnouin, O., Becker, T., Bottke, W., Boynton, W., et al., 2019. The unexpected surface of asteroid (101955) bennu. Nature 568 (7750), 55–60.
Leonovich, A., Gromov, V., Dmitriyev, A., Penetrigov, V., Senevov, P., Shvarev, V., 1977. The main peculiarities of the processes of the deformation and destruction of lunar soil. In: NASA, Washington the Soviet-Am. Conf. On Cosmochem. of the Moon and Planets. Pt. 2.
Metcalf, J., 1966. Angle of repose and internal friction. In: International Journal of Rock Mechanics and Mining Sciences & Geomechanics Abstracts, vol. 3, pp. 155–161. Elsevier.
Metzger, P.T., Britt, D.T., Covey, S., Schultz, C., Cannon, K.M., Grossman, K.D., Mantovani, J.G., Mueller, R.P., 2019. Measuring the fidelity of asteroid regolith and cobble simulants. Icarus 321, 632–646.
Miura, Y.N., Noguchi, T., Tsuchiyama, A., Yano, H., Yoshida, S., Nagata, K., 2008. Compressive strength measurements of meteorites and terrestrial rocks: implications for physical properties of asteroidal surfaces. In: Proceedings of the Japan Geoscience Union Meeting. P168-P002.
Miyamoto, H., Yano, H., Scheeres, D.J., Abe, S., Barnouin-Jha, O., Cheng, A.F., Demura, H., Gaskell, R.W., Hirata, N., Ishiguro, M., et al., 2007. Regolith migration and sorting on asteroid itokawa. Science 316 (5827), 1011–1014.
Omidvar, M., Iskander, M., Bless, S., 2012. Stress-strain behavior of sand at high strain rates. Int. J. Impact Eng. 49, 192–213.
Ostrowski, D., Bryson, K., 2019. The physical properties of meteorites. Planet. Space Sci. 165, 148–178.
Perko, H.A., Nelson, J.D., Sadeh, W.Z., 2001. Surface cleanliness effect on lunar soil shear strength. J. Geotech. Geoenviron. Eng. 127 (4), 371–383.
Poulos, H.G., Davis, E.H., 1980. Pile Foundation Analysis and Design. No. Monograph.
Pravec, P., Scheirich, P., Kušnirák, P., Šarounová, L., Mottola, S., Hahn, G., Brown, P., Esquerdo, G., Kaiser, N., Krzeminski, Z., et al., 2006. Photometric survey of binary near-earth asteroids. Icarus 181 (1), 63–93.
Rognon, P.G., Roux, J.-N., Naaim, M., Chevoir, F., 2008. Dense flows of cohesive granular materials. J. Fluid Mech. 596, 21–47.
Rozitis, B., MacLennan, E., Emery, J.P., 2014. Cohesive forces prevent the rotational breakup of rubble-pile asteroid (29075) 1950 da. Nature 512 (7513), 174–176.
Sánchez, D.P., Scheeres, D.J., 2012. DEM simulation of rotation-induced reshaping and disruption of rubble-pile asteroids. Icarus 218 (2), 876–894.
Sánchez, P., Scheeres, D., 2009. Granular Mechanics in Asteroid Regolith: Simulating and Scaling the brazil Nut Effects. LPI, p. 2228.
Sánchez, P., Scheeres, D.J., 2011. Simulating asteroid rubble piles with a self-gravitating soft-sphere distinct element method model. Astrophys. J. 727 (2), 120.
Sánchez, P., Scheeres, D.J., 2014. The strength of regolith and rubble pile asteroids. Meteoritics Planet Sci. 49 (5), 788–811.
Sánchez, P., Scheeres, D.J., 2016. Disruption patterns of rotating self-gravitating aggregates: a survey on angle of friction and tensile strength. Icarus 271, 453–471.
Sánchez, P., Scheeres, D.J., 2018. Rotational evolution of self-gravitating aggregates with cores of variable strength. Planet. Space Sci. 157, 39–47.
Scheeres, D.J., Hartzell, C.M., Sánchez, P., Swift, M., 2010. Scaling forces to asteroid surfaces: the role of cohesion. Icarus 210 (2), 968–984.
Schorghofer, N., 2008. The lifetime of ice on main belt asteroids. Astrophys. J. 682 (1), 697.
Sharma, I., 2013. Structural stability of rubble-pile asteroids. Icarus 223 (1), 367–382.
Shi, H., Mohanty, R., Chakravarty, S., Cabiscol, R., Morgeneyer, M., Zetzener, H., Ooi, J.Y., Kwade, A., Luding, S., Magnanimo, V., 2018. Effect of particle size and cohesion on powder yielding and flow. KONA Powder. Paticle J., 2018014
Silbert, L.E., Ertaş, D., Grest, G.S., Halsey, T.C., Levine, D., Plimpton, S.J., 2001. Granular flow down an inclined plane: bagnold scaling and rheology. Phys. Rev. 64 (5), 051302.
Slyuta, E., 2014. Physical and mechanical properties of the lunar soil (a review). Sol. Syst. Res. 48 (5), 330–353.
Sugita, S., Honda, R., Morota, T., Kameda, S., Sawada, H., Tatsumi, E., Yamada, M., Honda, C., Yokota, Y., Kouyama, T., et al., 2019. The geomorphology, color, and thermal properties of ryugu: implications for parent-body processes. Science 364 (6437).
Tsuchiyama, A., Mashio, E., Imai, Y., Noguchi, T., Miura, Y.N., Yano, H., 2008. Strength measurements of carbonaceous chondrites and cosmic dust analogs using micro compression testing machine. In: Japan Geosciences Union Meeting, Abstracts of Papers.
Walsh, K., Jawin, E., Ballouz, R.-L., Barnouin, O., Bierhaus, E., Connolly, H., Molaro, J., McCoy, T., Delbo, M., Hartzell, C., et al., 2019. Craters, boulders and regolith of (101955) bennu indicative of an old and dynamic surface. Nat. Geosci. 12 (4), 242–246.
Walsh, K.J., 2018. Rubble pile asteroids. Annu. Rev. Astron. Astrophys. 56, 593–624.
Walsh, K.J., Richardson, D.C., Michel, P., 2012. Spin-up of rubble-pile asteroids: disruption, satellite formation, and equilibrium shapes. Icarus 220 (2), 514–529.
Watanabe, S., Hirabayashi, M., Hirata, N., Hirata, N., Noguchi, R., Shimaki, Y., Ikeda, H., Tatsumi, E., Yoshikawa, M., Kikuchi, S., et al., 2019. Hayabusa2 arrives at the carbonaceous asteroid 162173 ryugu—a spinning top–shaped rubble pile. Science 364 (6437), 268–272.
Whitman, R.V., 1970. The response of soils to dynamic loadings; report 26, final report. Tech. rep.. In: MASSACHUSETTS INST OF TECH CAMBRIDGE DEPT OF CIVIL ENGINEERING.
Zhou, Z., Zou, R., Pinson, D., Yu, A., 2014. Angle of repose and stress distribution of sandpiles formed with ellipsoidal particles. Granul. Matter 16 (5), 695–709.